


Critical current density of superconducting-normal-superconducting Josephson junctions and polycrystalline superconductors in high magnetic fields

A. I. Blair* and D. P. Hampshire[†]

Superconductivity Group, Centre for Materials Physics, Department of Physics, Durham University, Durham DH1 3LE, United Kingdom

 (Received 6 October 2021; revised 1 March 2022; accepted 30 March 2022; published 16 May 2022)

We investigate the in-field critical current density $J_c(B)$ of superconducting-normal-superconducting (SNS) Josephson junctions (JJs) and polycrystalline superconducting systems with grain boundaries modeled as Josephson-type planar defects, both analytically and through computational time-dependent Ginzburg-Landau (TDGL) simulations in two and three dimensions. For very narrow SNS JJs, we derive analytic expressions for $J_c(B)$ that are high-field solutions for $J_c(B)$ for JJs across the entire applied field range up to the effective upper critical field B_{c2}^* . They generalize the well-known (low-field) exponential junction thickness dependence for J_c from de Gennes, often used in the Josephson relation. We then extend our analytic expressions to describe wider junctions using physical arguments, and we confirm their agreement with TDGL simulations. These results are then compared with the current densities found in superconductors optimized for high-field applications. They provide an explanation for the Kramer field dependence and inverse power-law grain size dependence widely found in many low-temperature superconductors, and the power-law field dependence $J_c(B) \sim B^{-0.6}$ found at intermediate fields in some high-temperature superconductors including powder-in-tube $\text{Bi}_2\text{Sr}_2\text{Ca}_2\text{Cu}_3\text{O}_x$ and $R\text{Ba}_2\text{Cu}_3\text{O}_7$ tapes (R = rare earth). By reanalyzing critical current density data using the mathematical framework derived here and confirmed using TDGL, we enable an analysis of J_c data that provides the local properties of grain boundaries in high-field superconductors and hence a deeper understanding of how grain boundaries influence J_c in high magnetic fields.

DOI: [10.1103/PhysRevResearch.4.023123](https://doi.org/10.1103/PhysRevResearch.4.023123)

I. INTRODUCTION

Probably the most important challenge in high-field superconductivity is to understand and control the critical current density J_c of superconducting materials in high magnetic fields. The enormous dissipationless currents that technological superconducting materials can carry have made them essential components in large-scale high-field magnet systems, such as those used for high-resolution nuclear magnetic resonance (NMR) or to confine fusion plasmas [1].

However, a quantitative description of J_c in high fields for these materials is limited by our understanding of the so-called “grand summation problem”: the problem of how the local vortex-vortex and vortex-pin interactions should be summed in order to obtain the macroscopic average J_c . For example, the proportion of vortices that are pinned at pinning sites, or how vortices relax after being depinned, remains unknown. Without such knowledge, our understanding of the vortex pinning and J_c remains qualitative at best and

has prevented us from relating J_c to the underlying spatially varying properties of superconductors with strong pinning, which is needed to further optimize these materials. Here, we follow those approaches that have used Josephson junctions (JJs) as analogs of grain boundaries for the basis of descriptions of flux flow and pinning in polycrystalline materials, computationally [2], and experimentally in both low and high-temperature superconductors [3–5]. There have been some high-field approximations proposed for very narrow junctions that lack vortices in the junction region [6,7]. However, to our knowledge, there are no detailed analytic expressions for J_c for JJ in high fields up to the effective upper critical field B_{c2}^* (of any width) that can address the complexity of vortices entering the superconducting electrodes [8,9]. Here, we provide an analytic framework that describes J_c in high fields up to B_{c2}^* for systems that have many vortices both inside the junctions and in the superconducting electrodes. Necessarily, our work solves the grand summation problem within the critical Josephson junction region itself, by including the nonuniform distribution of vortices in the junctions at J_c [8,10]. Our approach is to derive one-dimensional (1D) results for very narrow junctions and then use physical arguments to find expressions that describe J_c in wider junctions. In both cases, we confirm the validity of the expressions produced using time-dependent Ginzburg-Landau (TDGL) simulations. TDGL theory has been used to model the critical current density as a function of applied field for a wide range of superconducting systems that contain normal material [2,11–14].

*Present address: United Kingdom Atomic Energy Authority, Culham Science Centre, Abingdon, Oxfordshire, United Kingdom; alexander.blair@ukaea.uk

[†]d.p.hampshire@durham.ac.uk

Published by the American Physical Society under the terms of the Creative Commons Attribution 4.0 International license. Further distribution of this work must maintain attribution to the author(s) and the published article's title, journal citation, and DOI.

We first outline the computational method used to obtain critical current density as a function of applied field and validate it against the canonical low-field expressions for the critical current density of junctions. We then present our analytic solutions for the critical current density of very narrow superconducting-normal-superconducting (SNS) junctions in all applied magnetic fields up to the upper critical field of the system, by extending the approach of Fink used in low fields [15] and developing the methodology of Refs. [16,17] to account for the suppression of superconductivity in the superconducting electrodes in high fields. Next, we use physical arguments to extend these very narrow width in-field expressions for critical current density to describe wider, so-called narrow JJs, up to the scale of λ_s , and confirm their agreement with TDGL. Finally, we present 3D TDGL simulations and visualizations of equiaxed polycrystalline systems with grain boundaries that are SNS Josephson junctions. We discuss the qualitative agreement between the 3D TDGL simulations, the analytic expressions derived, and the widely observed experimental results for $J_c(B_{\text{app}})$, namely, the Kramer dependence [18] for low-temperature superconductors such as Nb_3Sn [19,20], Nb_3Al [21], and PbMo_6S_8 [22] throughout most of the magnetic field range, and the power-law dependence [i.e., $J_c(B_{\text{app}}) \sim B_{\text{app}}^{-0.6}$] observed at intermediate fields of several teslas for several high-temperature superconductors such as powder-in-tube $\text{Bi}_2\text{Sr}_2\text{Ca}_2\text{Cu}_3\text{O}_x$ [23] and $\text{RBa}_2\text{Cu}_3\text{O}_7$ tapes [5].

II. TIME-DEPENDENT GINZBURG-LANDAU THEORY

In this paper, we analyze Josephson junction systems entirely within the framework of the TDGL equations for gapless s -wave superconductors in the dirty limit [24], which can be written as [25,26]

$$\eta(\partial_t + \iota\mu)\psi = \left[\sum_i (\partial_i - \iota A_i) m_i^{-1}(\mathbf{r})(\partial_i - \iota A_i) + \alpha(\mathbf{r}) - \beta(\mathbf{r})|\psi|^2 \right] \psi, \quad (1)$$

$$\partial_t A_i + \partial_i \mu = -\kappa^2 m_i(\mathbf{r})(\nabla \times \nabla \times \mathbf{A})_i + \text{Im}[\psi^*(\partial_i - \iota A_i)\psi], \quad (2)$$

where $\iota = \sqrt{-1}$ is the imaginary unit; we take the (real) dirty-limit value of $\eta = 5.79$ obtained by Schmid [27], and all other parameters have their usual meaning. For simplicity, we shall take $m_i(\mathbf{r})$ and $\alpha(\mathbf{r})$ to be the only spatially varying material-dependent parameters and assume the nonlinearity parameter β to be constant across the system. The condensation term α is expressed in terms of the system temperature T and the local critical temperature $T_c(\mathbf{r})$ relative to the critical temperature of the reference superconductor $T_{c,s}$ as

$$\alpha(\mathbf{r}) = \frac{T - T_c(\mathbf{r})}{T - T_{c,s}} \quad (3)$$

such that α is unity in the reference superconductor and negative in normal (nonsuperconducting) materials. The associated

boundary conditions are

$$(\nabla \times \mathbf{A} - \mathbf{B}_{\text{app}}) \times \hat{\mathbf{n}} = \mathbf{0}, \quad (4)$$

$$(\nabla - \iota \mathbf{A})\psi \cdot \hat{\mathbf{n}} = -\Gamma_{\text{DG}}\psi, \quad (5)$$

where the surface parameter Γ_{DG} is the reciprocal of de Gennes's extrapolation length in units of the coherence length [28] and has the limiting values of 0 for an interface with an insulating surface (or vacuum) and $\pm\infty$ for the interface with a highly conductive surface [29].

However, for many systems of experimental interest that operate in high magnetic fields, Eqs. (1) and (2) are computationally expensive to solve, and a further mathematical simplification is needed for 3D simulations. Fortunately, in all high-field materials, the (effective) penetration depth is often much larger than all other length scales in the system, and the self-field can be neglected relative to the applied magnetic field and current densities, such that the TDGL equations in the high- κ limit apply [25]. In this high- κ approximation, for an applied magnetic field B_{app} in the z direction, the normalized magnetic vector potential in the Coulomb gauge ($\nabla \cdot \mathbf{A} = 0$) is expressed as $\mathbf{A} = -B_{\text{app}}(y - w/2)\hat{\mathbf{i}} - \mathbf{K}$, where $\mathbf{K} = K(t)\hat{\mathbf{i}}$ is a spatially invariant parameter required to enforce the Coulomb gauge constraint and w is the width of the system in the y direction. The gauge constraint \mathbf{K} can be used to determine the average electric field across the domain, since $\partial_t \mathbf{K} = \langle \mathbf{E} \rangle$. The only spatially dependent material parameter in this model is $\alpha(\mathbf{r})$. This formulation is particularly useful for our 3D simulations of superconducting systems as the time dependence of the electromagnetic fields is coupled only through the spatially invariant gauge parameter \mathbf{K} , reducing the computational cost of developing the superconducting state in time [25].

III. NUMERICAL METHODS FOR SOLVING THE TDGL EQUATIONS FOR JUNCTION SYSTEMS

In this paper we use two main simulation codes to solve the TDGL equations for SNS junction systems in simple geometries. For small system sizes in 2D, we will solve the general equations (1) and (2) using our TDGL-2D code, based on the algorithm developed by Refs. [30,31]. We apply the "link variable" approach used in the explicit method [32] together with the semi-implicit spatial discretization scheme for the TDGL equations [31] that is generalized to include a spatially dependent effective mass. However, although the time evolution of the order parameter ψ is carried out using an adapted version of the Crank-Nicolson algorithm [31], the two components of the magnetic vector potential are then developed in time simultaneously for greater stability when simulating systems with low κ . For larger systems, and in 3D, we shall solve the simplified TDGL equations in the high- κ limit, on a graphics processing unit (GPU) using our TDGL-HI κ code, an implementation of the 3D TDGL solver developed in Ref. [25]. For evolving $\{a, \psi\}$ (where a is a link variable associated with the magnetic vector potential), the adapted Crank-Nicolson algorithm [31] is known to be

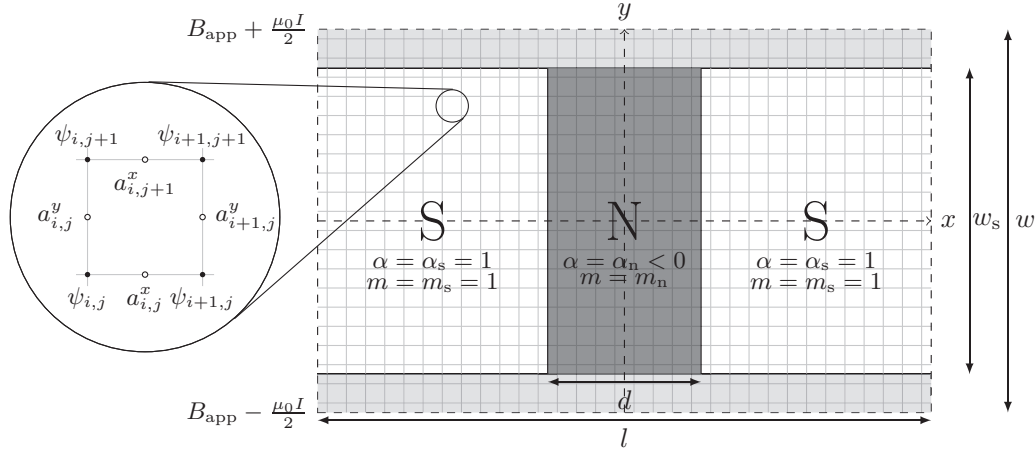


FIG. 1. Schematic of the 2D computational domain of width w and periodic length l used to model the junction system. The domain is subdivided into three sections; the main superconducting region, S, in which the normalized Ginzburg-Landau temperature parameter $\alpha = 1$ and normalized effective mass $m = 1$, a normal region, N, described by the normalized Ginzburg-Landau temperature parameter and effective mass α_n and m_n , respectively, and a coating region, marked in light gray, in which $\alpha = -10.0$ and $m = 10^8$ when modeling junctions with insulating coatings. The applied field B_{app} and current I are controlled by fixing the local magnetic field at the edges of the computational domain in the y direction. The junction thickness in the direction of current flow is denoted d , and the junction width is denoted w_s . Exploded view: the discretized order parameter $\psi_{i,j}$ and modified link variables $a_{i,j}^x$ and $a_{i,j}^y$ relative to the underlying computational grid. Unless otherwise stated, the grid step size is typically taken to be $h_x = h_y = 0.5\xi_s$ in these simulations.

unconditionally stable for purely linear sets of equations [33], although stability is not guaranteed in the nonlinear case. Unlike the explicit scheme of Gropp *et al.* [32], which uses the computational variables $\{U\} = \{\exp(-\iota a)\}$ instead of $\{a\}$ directly, numerical errors of schemes based on Ref. [31] will increase for long simulations of periodic systems in resistive states, as the magnitude of $\{a\}$ can grow large over time and slow or even prevent convergence. However, as we are predominantly interested in the critical current density J_c and the onset of persistent resistive states in the system, this does not significantly limit the simulations presented here, and this consideration is outweighed by the reduction in simulation time possible using the longer time steps that the Crank-Nicolson approach permits as a result of its greater stability properties. Computation efficiencies were achieved by solving Eq. (1) directly in two steps using the method of fractional steps. We also avoided solving Eq. (2) in two iteration steps [31], as the timescales for the evolution of $\{a^x\}$ and $\{a^y\}$ are of similar magnitudes, and in these calculations led to oscillatory behavior of the iteration scheme with a block Gauss-Seidel approach and unreliability of convergence [33]. Convergence was considered satisfied when changes in the normalized link variable and order parameter were $< 10^{-7}$ at each time step.

Typically, TDGL-2D is used to solve the TDGL equations for systems that are periodic in the direction of current flow in the x direction with periodicity l , and bounded in the y direction with a width w such that $y \in [-\frac{w}{2}, \frac{w}{2}]$, at the extremities of which we impose the insulating boundary condition $\Gamma_{\text{DG}} = 0$ using Eq. (5). A schematic of the computational grid and the relevant dimensions used are presented in Fig. 1 for the system used to model a typical periodic array of SNS junctions each of thickness d . Inside this domain, we specify three regions: a superconducting region of width w_s where $(|y| < \frac{w_s}{2}, |x| > \frac{d}{2})$ and in which $\alpha(\mathbf{r}) = m_i(\mathbf{r}) = 1$; a junction

region $(|y| < \frac{w_s}{2}, |x| < \frac{d}{2})$ in which $\alpha(\mathbf{r}) = \alpha_n$ and $m_i(\mathbf{r}) = m_n$; and a coating region $(\frac{w_s}{2} < |y| < \frac{w}{2})$ of width $w_{\text{coat}} = (w - w_s)/2$ either side of the junction in which $\alpha(\mathbf{r}) = \alpha_{\text{coat}}$ and $m_i(\mathbf{r}) = m_{\text{coat}}$. For the 2D simulations presented in this paper, $w_{\text{coat}} = 5.0\xi_s$, $\alpha_{\text{coat}} = -10.0$, and $m_{\text{coat}} = 10^8 m_s$ unless otherwise specified.

In order to extract values for the critical current density J_c , we followed the experimental approach [34] and used an arbitrary electric field criterion E_c written in terms of E_D , which corresponds to the average electric field in the system when the superconductor is normal and carrying the zero-field Ginzburg-Landau depairing current density J_D , such that

$$E_D = \kappa^2 \rho_{\text{av}}^x J_D, \quad (6)$$

where

$$\rho_{\text{av}}^x = \frac{w}{w_s} \frac{1}{n_x} \sum_{i=1}^{n_x} \frac{n_y}{\sum_{j=1}^{n_y} [(m^{-1})_{i,j}^x]}, \quad J_D = \frac{2}{3\sqrt{3}} J_0, \quad (7)$$

where ρ_{av}^x represents the average resistivity of the system in the x direction, normalized to the resistivity of a system in the x direction containing only the superconductor in its normal state. The supercurrent J^s is normalized in units of $J_0 = B_{c2}/\kappa^2 \mu_0 \xi_s$, where μ_0 is the permeability of free space, and the electric field is normalized in units of $J_0 \rho_s$. As the critical current density of the superconductor can be highly hysteretic, the system was always first initialized in the Meissner state throughout ($\psi = 1$, $\mathbf{A} = 0$) for all simulations. The external magnetic field $B(y = \pm \frac{w}{2})$ was then increased at a rate of $5 \times 10^{-2} B_{c2} \tau^{-1}$ up to the desired value B_{app} . Following this magnetic field ramp, for our 2D (3D) simulations the applied current density J_{app} was increased (decreased) in a

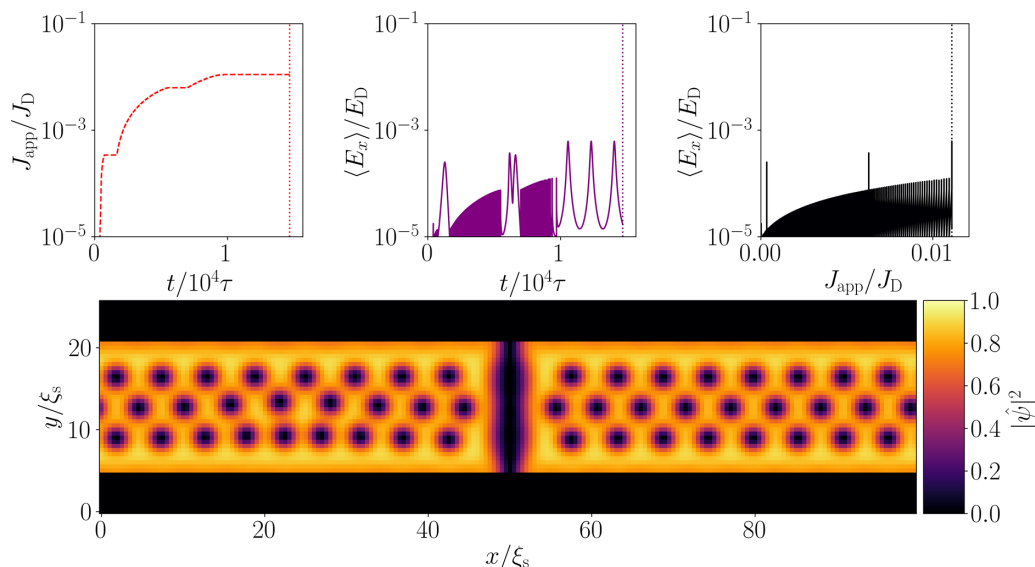


FIG. 2. Typical simulation data used to extract J_c at the applied field $B_{\text{app}} = 0.3B_{c2}$. Bottom: distribution of the normalized Cooper pair density $|\tilde{\psi}|^2$ at the critical current J_c , for a simulated junction with periodic length $l = 100\xi_s$, thickness $d = 0.5\xi_s$, junction width $w_s = 16.0\xi_s$, and Ginzburg-Landau temperature parameter in the normal region $\alpha_n = -20$. Top left: The applied current density J_{app} normalized by the depairing current density J_D vs time t normalized in units of the characteristic timescale τ . Top center: The average electric field in the x direction $\langle E_x \rangle$ normalized by the characteristic electric field E_D as a function of time t . Top right: The normalized average electric field in the x direction as a function of the applied current density. The applied current density when $E < E_c = 10^{-5}E_D$, and J_c is determined as the lowest current at which $E > E_c$ for a duration exceeding $t_{\text{hold}} = 5 \times 10^3\tau$.

series of logarithmically spaced steps, starting from $10^{-6}J_D$. If the average electric field in the system exceeded the electric field criterion, typically $E_c = 10^{-5}E_D$, the applied current was held constant. When the average electric field continued to persist above E_c for longer than the hold time t_{hold} , typically taken as $5 \times 10^4\tau$, the system was determined to have entered a persistent resistive state, and J_{app} at this point is taken to be the critical current density of the system.

An example of the time evolution of the applied current density and average electric field used to extract J_c from the simulation is displayed in Fig. 2. The rapid jumps in the average electric field in the system $\langle E_x \rangle$ below the critical current ($t < 1.1 \times 10^4$) are associated with the imposed current steps and the associated steps in the rate of change of the magnetic field in the system. To make the generation of a full $J_c(B_{\text{app}})$ characteristic more efficient, we also simulate J_c at different applied fields in parallel, since the simulations for the critical current at given applied fields are independent of one another.

For the computationally expensive 3D systems, we use TDGL-HI κ using the scalable GPU accelerated algorithm developed in Ref. [25]. The order parameter ψ , the electrostatic potential μ , and the gauge parameter K are updated successively at each time step, with ψ and μ solved for iteratively as described in Ref. [25] until $|\psi_{n+1} - \psi_n|^2 < 10^{-5}$ and $|\nabla^2\mu - \nabla \cdot \text{Im}[\psi^*(\nabla - i\mathbf{A})\psi]|^2 < 10^{-5}$ at every mesh point. K is integrated forward in time using a second-order Runge-Kutta algorithm [35]. Local order parameter fluctuations were also included and set to be sufficiently small so as to minimize creep effects that may complicate the determination of J_c and correspond to nearly zero thermal noise for vortex flow [36], but sufficiently large to speed up relaxation of the order parameter when the system is out of equilibrium, such as

immediately after initialization. Insulating or (quasi)periodic boundary conditions can be applied at the edges of the simulation domain in any (or all) spatial dimensions [25]. For a periodic domain of size L_x, L_y, L_z in the $x, y,$ and z dimensions, respectively, with a magnetic field applied along the z axis, periodic boundary conditions can be applied to ψ at the edges of the domain in the x and z dimensions, and quasiperiodic boundary conditions (QBCs) on ψ in the y dimension, as described in Ref. [25] (and not implemented in previous work [37]), were used to eliminate surface effects from masking bulk critical currents. For 3D simulations, we follow the J_c determination method employed in Ref. [38], and ramp the applied current down in steps from the resistive to the superconducting state. At each current step, the current is held for t_{hold} , and the spatially averaged electric field in the superconductor E_x is averaged over the second half of the hold step, after transient effects from stepping the current have decayed away. Typically, $t_{\text{hold}} = 10.0\tau$. The critical current density J_c is then taken to be the highest current at which the time-averaged and spatially averaged E_x is less than the electric field criterion $E_c = 10^{-5}\rho J_0$.

IV. WEAKLY COUPLED SNS JUNCTIONS IN MAGNETIC FIELDS ($\alpha_n d \gg \xi_s$)

Following Clem's consideration of films, Eqs. (1) and (2) can be rewritten in terms of gauge-invariant variables: the Cooper pair density $|\psi|^2$, the (super)current density \mathbf{J}^s , and the gauge-invariant phase γ [8]. When $m_i(\mathbf{r}), \alpha(\mathbf{r}), \beta(\mathbf{r})$ are only functions of x , and solutions for the order parameter are considered in the form $\psi = |\psi|e^{i\theta}$, where θ is the (non-gauge-invariant) phase of the order parameter, the time-independent

Ginzburg-Landau (GL) equations are [16]

$$\left[\sum_i \left(\partial_i [m_i^{-1}(x) \partial_i] - m_i^{-1}(x) (\partial_i \gamma)^2 \right) + \alpha(\mathbf{r}) - \beta(\mathbf{r}) |\psi|^2 \right] |\psi| = 0, \quad (8)$$

$$\mathbf{J}^s = m_i^{-1}(x) |\psi|^2 \nabla \gamma, \quad (9)$$

where

$$\nabla \gamma = \nabla \theta - \mathbf{A}. \quad (10)$$

Although Clem's original work was developed for thin films, it remains valid for the narrow 2D systems considered here since in both cases, ψ is independent of z and the local magnetic field can be taken to be equal to the applied field as $w < \lambda_s$. Clem's low-field solutions for the gauge-invariant phase difference $\Delta\gamma(y)$ and average critical current density across a narrow junction [8] are given by

$$\Delta\gamma(y) = \Delta\gamma(0) + B_{\text{app}} y d_{\text{eff}} + \frac{8B_{\text{app}}}{w_s} \sum_{n=0}^{\infty} \frac{(-1)^n}{k_n^3} \times \tanh(k_n l_s / 2) \sin(k_n y), \quad k_n = (2n + 1)\pi / w_s, \quad (11)$$

$$J_c = \max_{\varphi(0)} \left\{ \frac{1}{w_s} \left| \int_{-w_s/2}^{w_s/2} dy [J_{\text{DJ}}(0) \sin[\Delta\gamma(y)]] \right| \right\}, \quad (12)$$

where $J_{\text{DJ}}(0)$ is the current density in zero field. In this case, $\gamma(0) = \pm\pi/2$ when the current through the junction is maximized for all ratios of l_s/w_s [8]. In order to improve agreement between our computation and Eq. (11), we have included a term for the effective junction thickness d_{eff} (which we find below to be $d_{\text{eff}} \approx 2\xi_s$ in the weak-coupling limit). This term accounts for the finite size of the junction and the reduction in the order parameter on a length scale of order ξ_s close to the junction. This addition better describes thin junctions (i.e., the limit considered in Ref. [8]). For consistency, we define the effective length of the S regions in the direction of current flow to be $l_s = l - d_{\text{eff}}$.

To identify the fraction of the width contributing to the *net* critical current, we suggest that the maxima of Eq. (12), J_c^{peak} , can be approximated using

$$J_c^{\text{peak}} \approx c_0 \left(\frac{\phi_0}{B w_s^2} \right)^{c_1} J_{\text{DJ}}(0). \quad (13)$$

We find empirically that over a large range of aspect ratios, the field dependence of J_c^{peak} most closely follows the Bessel function field dependence, where, for example, when $w_s \approx l_s$, $c_0 \approx c_1 \approx 0.6$, the distance between the cores of the vortices in the junction, a_j , is given by $a_j \approx 1.84\phi_0/B_{\text{app}}w_s$ and over a range of aspect ratios for the electrodes, $c_0 \approx 0.35/c_1$ is quite robust. As noted in Refs. [10,39], the reduction of the critical current with applied field when many vortices are present in the junction is slower when $w_s \ll l_s$ and the asymptotic behavior is a Bessel-like function where $J_c \sim B_{\text{app}}^{-1/2}$, compared with when $l_s \ll w_s$ and a sinc-like behavior $J_c \sim B_{\text{app}}^{-1}$ is found.

A comparison between the critical current density determined from Eqs. (11) and (12) and the critical current density

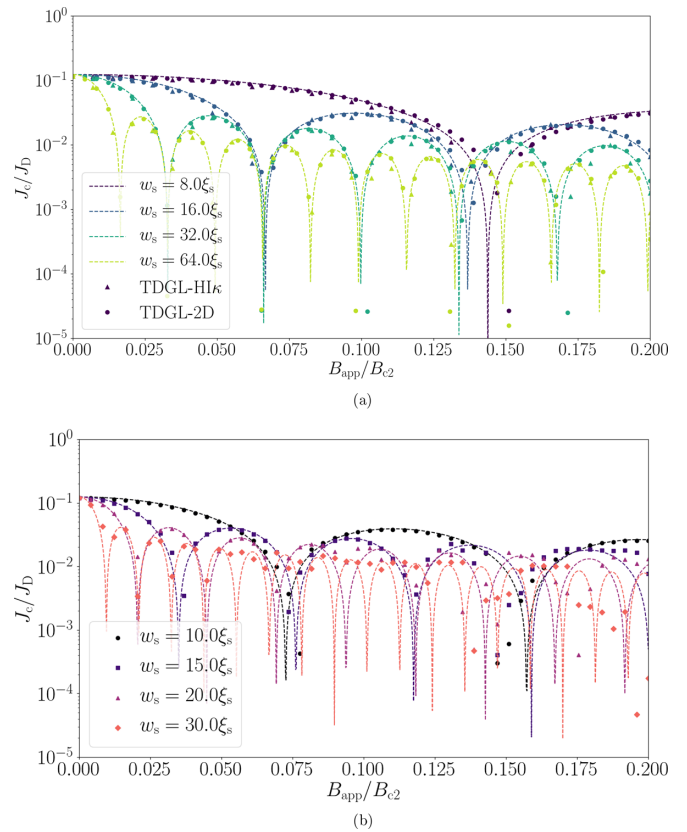


FIG. 3. Simulations of $J_c(B)$ of narrow, very thin, weakly coupled junctions with different widths w_s . The system size in the x direction is $l = 6.0\xi_s$ (a) and $100.0\xi_s$ (b). The junction thickness d was taken to be $d_{\text{min}} = 0.5\xi_s$, $\alpha_n = -20.0$, and $\kappa = 40.0$. (a) $J_c(B)$ as calculated using the TDGL-2D code (circles) and TDGL-HI κ code (triangles), with the hold time and time step for the TDGL-2D simulations set to $t_{\text{hold}} = 5 \times 10^3 \tau$ and $\delta t = 0.5 \tau$, and for the TDGL-HI κ simulations set to $t_{\text{hold}} = 10 \tau$ and $\delta t = 0.1 \tau$, respectively. (b) $J_c(B)$ as calculated using the TDGL-2D code with hold time $t_{\text{hold}} = 10^3 \tau$ and time step 0.1τ . Dashed lines in both panels are given by Eqs. (11) and (12) with $d_{\text{eff}} = 2\xi_s$.

obtained from our 2D TDGL simulations is shown in Fig. 3 for a system with $w_s \gg l_s$ [Fig. 3(a)] and $w_s \ll l_s$ [Fig. 3(b)]. In both cases, we take $d_{\text{eff}} \approx 2\xi_s$. The 2D TDGL simulations J_c from both TDGL-2D and TDGL-HI κ show excellent agreement with each other and the analytic expressions derived from Eqs. (11) and (12) in low fields. At these applied fields, no vortices exist in the S regions, and current flow is laminar within them. In Fig. 3(b), simulations of J_c obtained from TDGL-2D for larger system widths at $B = 0.2B_{c2}$ still follow the prediction of Eqs. (11) and (12), but with larger scatter as a consequence of vortices in the S regions that distort the interference pattern of the computed system from the analytic prediction [39].

For completeness, we checked our results against a smaller grid step size $0.1\xi_s$ and confirmed little change in $J_c(B)$ values. Throughout this paper, a standard grid step size of $0.5\xi_s$ was chosen since it gave the optimal trade-off between accuracy and computation time. We also checked the sensitivity of the results in this section to having a highly resistive coating, rather than an insulator, at the edges of the

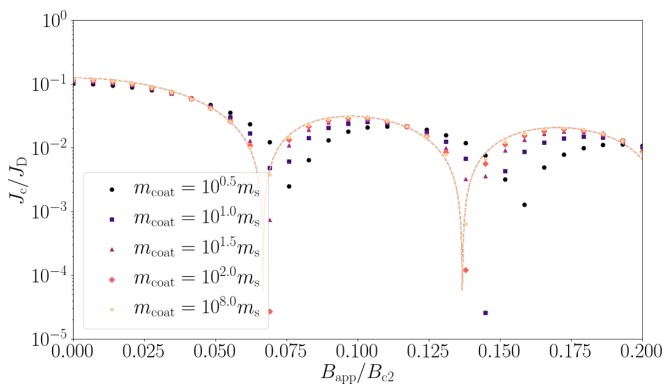


FIG. 4. Simulations of the critical current of a very thin junction in the weak-coupling limit with the Ginzburg-Landau temperature parameter in the normal region $\alpha_n = -20.0$, a junction thickness $d = 0.5\xi_s$, smaller than the superconducting coherence length ξ_s , and a width $w_s = 16\xi_s$ much smaller than the Josephson penetration depth λ_J for varying coating effective mass (proportional to the coating resistivity) with a coating thickness of $5\xi_s$. The periodic system size in the x direction is $l = 6.0\xi_s$, and the Ginzburg-Landau parameter and friction coefficient in the superconductor are $\kappa = 40.0$ and $\eta = 5.79$, respectively, throughout. For this system, coating masses below $\sim 30m_s$ show distortion of the Fraunhofer pattern, with reduced zero-field J_c and increased spacing between minima in the J_c characteristic relative to the insulating coating limit ($m_{\text{coat}} \rightarrow \infty$). Remaining computational parameters are as described in the text. The dashed line is given by Eqs. (11) and (12) with $d_{\text{eff}} = 2\xi_s$.

junction system. This coating allows the order parameter at the superconductor/coating interface to decay into the coating region which affects the critical current characteristics in field. The simulation data shown in Fig. 4 show that insulating surface conditions are found if the effective mass in the coating material is greater than around 30 times the maximum effective mass in the rest of the system.

A. Very narrow junctions in high fields

In this section, we derive analytic expressions for the critical current density of very narrow Josephson junctions ($w < \xi_s$) that are valid across the entire range of applied magnetic fields, up to the upper critical field of the system. Consider first the current flow within the junction from screening currents and from the injected currents. Integrating around a thin closed rectangular loop inside the system using Eq. (10) with the lower path along the x axis and the upper path at y gives

$$\oint \nabla \gamma \cdot d\mathbf{l} = \oint \nabla \theta \cdot d\mathbf{l} - \oint \mathbf{B} \cdot d\mathbf{S} \quad (14)$$

after applying Stokes's theorem to the magnetic vector potential term. For any choice of gauge, the first closed integral on the right-hand side in θ is $2\pi n$, where n is the number of vortex cores inside the closed contour, from the requirement that the order parameter magnitude be a single valued function. We can integrate Eq. (8) over the junction width in the y direction, apply the mean value theorem, and replace ψ with its average in the y direction $f = \frac{1}{w} \int_{-w/2}^{w/2} |\psi| dy$ and the components of \mathbf{J}^s by their equivalent average $\langle j_i^s \rangle = \frac{1}{w} \int_{-w/2}^{w/2} (J_i^s) dy$. We as-

sume that the order parameter magnitude is symmetric about both the y axis and the x axis, that the screening currents and hence $\partial_y \gamma$ are both antisymmetric about these axes, and that to first order the transport current is uniform along the y axis, such that $\langle j_x^s \rangle = m_x^{-1}(x) f^2 \partial_x \gamma(y=0)$ from Eq. (9). Given that no vortex cores exist in the narrow system ($n = 0$), and taking the sections of the contour in Eq. (14) that are parallel to the x axis to be sufficiently short relative to the coherence length ξ , we arrive at the gauge-invariant result

$$\partial_x \gamma(y) - \frac{\langle j_x^s \rangle}{f^2 m_x^{-1}(x)} = \frac{B_{\text{app}} y}{B_{c2} \xi_s}. \quad (15)$$

We also assume that for narrow junctions, given the boundary conditions at the insulating surfaces and the requirement for current continuity across the S-N internal interface, $j_y^s(x)$ can be taken to be zero. Equation 15 describes the transport current density and the screening currents that flow within the junction itself. We have not included the small self-field corrections to the net field, which describe the currents associated with a vortex-antivortex pair at the edges, since we assume that the self-field is much smaller than the applied field. Substituting our new expression for $\partial_x \gamma(y)$ into Eq. (8) and averaging over the y direction gives

$$\partial_x (m_x^{-1}(x) \partial_x f) + \left[\alpha(x) - m_x^{-1} q^2 - \beta(x) f^2 - \frac{\langle j_x^s \rangle^2}{f^4 m_x^{-1}(x)} \right] f = 0, \quad (16)$$

where $q^2 = (\frac{B_{\text{app}} w_s}{\sqrt{12} B_{c2} \xi_s})^2$. Equation 16 represents a generalization of Fink's zero-field results for very narrow junctions to all applied fields B_{app} . We can now solve for the critical current when the N region is thin (i.e., $d \ll \xi_s$) and when the N region is thick (i.e., $d \gg \xi_s$).

1. Thin junctions in high fields $d \ll \xi_s$

Consider first the thin-junction limit, where $d \ll \xi_s$. Assuming that $\beta(x)$ and $m_x^{-1}(x)$ are constant across the system for simplicity, we rescale Eq. (16) by $\tilde{x} = x\sqrt{1-q^2}$, $\tilde{f} = f/\sqrt{1-q^2}$, and $\tilde{j}_x = \langle j_x^s \rangle (1-q^2)^{-3/2}$ to give

$$\partial_{\tilde{x}} \tilde{f} + \left[1 - \frac{1 - \alpha(x)}{1 - q^2} - \tilde{f}^2 - \frac{\tilde{j}_x^2}{\tilde{f}^4} \right] \tilde{f} = 0. \quad (17)$$

Since \tilde{f} and \tilde{j}_x are continuous across the S/N interface, we find a constraint between $\partial_{\tilde{x}} \tilde{f}$ and \tilde{f} at the interface in the limit where $d \ll \xi_s$, by integrating Eq. (17) across the normal region, where $|\tilde{x}| < d\sqrt{1-q^2}/2$, and assuming that \tilde{f} is symmetric across the junction:

$$2\tilde{f}'_{d/2} = d \frac{1 - \alpha_n}{\sqrt{1 - q^2}} \tilde{f}_{d/2}, \quad (18)$$

where $\tilde{f}_{d/2} = \tilde{f}(x = d/2)$ and $\tilde{f}'_{d/2} = \partial_{\tilde{x}} \tilde{f}(x = d/2)$. The remainder of the derivation now follows the zero-field approach [40]; by substituting Eq. (18) into Eq. (17) and neglecting the highest-order terms in the new small parameter $V_0^{-1} = \sqrt{1 - q^2}/d(1 - \alpha_n)$, we find the necessary condition for a solution to exist as $\tilde{j}_x < 1/2V_0$. In standard units, this

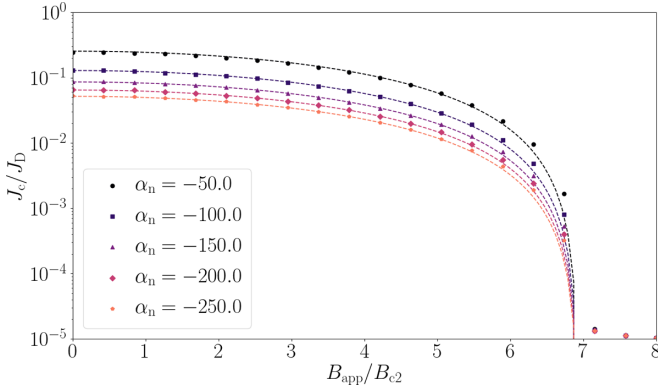


FIG. 5. Simulations of $J_c(B)$ of very narrow, thin, weakly coupled junctions as a function of α_n where $-250 \leq \alpha_n \leq -50$. The width $w_s = 0.5\xi_s$, and the junction thickness $d = d_{\min} = 0.1\xi_s$. The periodic system length in the x direction $l = 12.0\xi_s$, and $\kappa = 5$. The effective mass in the normal region was taken to be $m_n = m_s$. The grid spacing was chosen to be $h_x = h_y = 0.1\xi_s$, the time step $\delta t = 0.5\tau$, and the hold time $t_{\text{hold}} = 5 \times 10^3\tau$. Dashed lines are given by Eq. (19).

corresponds to the critical current density J_{DJ} ,

$$\lim_{d \ll \xi_s} \{J_{\text{DJ}}(B_{\text{app}})\} = J_0 \frac{\xi_s}{2d(1 - \alpha_n)} (1 - q^2)^2, \quad (19)$$

where $q^2 = (B_{\text{app}} w_s / \sqrt{12} B_{c2} \xi_s)^2$ and $J_0 = B_{c2} / \kappa^2 \mu_0 \xi_s$ as before. The applied field at which the critical current density of the system is zero is given by $q^2 = 1$. This is equivalent to an applied field equal to the parallel critical field

$$B_{\text{app}}(q^2 = 1) = \frac{\sqrt{12} \xi_s}{w_s} B_{c2}. \quad (20)$$

This expression has previously been found by Tinkham to be the upper critical field of a thin-film superconductor of thickness w_s when the applied magnetic field is parallel to the film surface, provided the film is thinner than approximately $1.8\xi_s$ [41]. Equation 19 is compared with simulation data from TDGL-2D in Fig. 5, showing excellent agreement across the whole field range.

We note that the junctionless case, where $V_0 = 0$, can trivially be considered also, as the rescaling used in Eq. (17) is equivalent to rescaling the Ginzburg-Landau equations in terms of a field-dependent coherence length in the superconductor $\tilde{\xi}_s = \xi_s / \sqrt{1 - q^2}$. In this case, the critical current of the thin-film system becomes $J_D(1 - q^2)^{3/2}$ [41].

2. Thick junctions in high field $d \gg \xi_s$

For thick junctions, we rescale Eq. (16) into a similar form to that studied for zero field by Fink [15]. In the superconducting regions, we rescale by $\tilde{x} = x\sqrt{1 - q^2}$, $\tilde{f}_s = f/\sqrt{1 - q^2}$, and $\tilde{j}_x = \langle j_x^s \rangle (1 - q^2)^{-3/2}$ to give

$$\partial_{\tilde{x}}^2 \tilde{f}_s + \left[1 - \tilde{f}_s^2 + \frac{\tilde{j}_x^2}{\tilde{f}_s^4} \right] \tilde{f}_s = 0. \quad (21)$$

Inside the normal region, we rescale Eq. (16) by $\tilde{u} = x\sqrt{\frac{m_n}{m_s}(-\alpha_n + \frac{m_s}{m_n}q^2)}$, $\tilde{f}_n = -f\sqrt{\beta_n/(-\alpha_n + \frac{m_s}{m_n}q^2)}$, and

$\tilde{j}_u = \langle j_x^s \rangle \beta_n \sqrt{m_n/m_s} (-\alpha_n + \frac{m_s}{m_n}q^2)^{-3/2}$ to give a form that is again similar to Fink's zero-field results,

$$-\partial_{\tilde{u}}^2 \tilde{f}_n + \left[1 - \tilde{f}_n^2 + \frac{\tilde{j}_u^2}{\tilde{f}_n^4} \right] \tilde{f}_n = 0. \quad (22)$$

The critical current in field can now be obtained following the procedure used by Ref. [15] for zero field, but with the new, field-dependent rescaled variables. In usual units, the critical current of this narrow junction system in applied fields is given by

$$\lim_{d \gg \xi_s > w_s} \{J_{\text{DJ}}(B_{\text{app}})\} = 4J_0(1 - q^2)^{\frac{3}{2}} \frac{1 - \sqrt{1 - \tilde{s}\tilde{f}_{d/2}^2}}{\tilde{s}\tilde{v}} \times \exp\left(-\frac{d}{\tilde{\xi}_s}\right), \quad (23)$$

where

$$\tilde{f}_{d/2}^2 = \frac{\tilde{v}^2 + 1 - \sqrt{\tilde{v}^2(2 - \tilde{s}) + 1}}{\tilde{v}^2 + \tilde{s}}, \quad \tilde{v} = \frac{m_n \tilde{\xi}_n}{m_s \xi_s} \sqrt{1 - q^2},$$

$$q^2 = \frac{B_{\text{app}}^2 w_s^2}{12}, \quad \tilde{s} = \frac{\beta_n(1 - q^2)}{(\alpha_n - \frac{m_s}{m_n}q^2)},$$

$$\times \tilde{\xi}_n = \sqrt{\frac{m_s}{m_n} \frac{1}{(-\alpha_n + \frac{m_s}{m_n}q^2)}} \xi_s, \quad (24)$$

and $J_0 = B_{c2} / \kappa^2 \mu_0 \xi_s$. Once again, here we take $\beta_n = 1$, and so when the effective mass of the N region is the same as that of the superconductors, $\tilde{v}^2 \rightarrow -\tilde{s}$, and $\tilde{f}_{d/2}^2 \rightarrow (1 - q^2)/2(1 - \alpha_n)$. Equation 23 is compared with the critical current densities obtained from TDGL-2D in Fig. 6. Excellent agreement between Eq. (23) and TDGL-2D is observed across the entire field range, and across the parameter space for $d > \xi_s$, $\alpha_n < -1.0$, and $0.1m_s < m_n < 6.0m_s$.

In the limit where $\tilde{f}_{d/2}^2 \rightarrow 0$, and when $m_n = m_s$, Eq. (23) reduces to the simpler form

$$\lim_{d \gg \xi_s > w_s} \{J_{\text{DJ}}(B_{\text{app}})\} = J_0 \frac{(1 - q^2)^2}{\sqrt{1 - \alpha_n}} \exp\left(-\frac{d\sqrt{1 - \alpha_n}}{\xi_s}\right), \quad (25)$$

which provides the general field-dependent form for de Gennes's famous result for SNS junctions in zero field [42]. In general, weakly coupled junctions with $\tilde{f}_{d/2}^2 \rightarrow 0$ for any thickness of junction with $m_n = m_s$ can be described by the single expression

$$\lim_{\xi_s > w_s} \{J_{\text{DJ}}(B_{\text{app}})\} = J_0 \frac{(1 - q^2)^2}{2\sqrt{1 - \alpha_n} \sinh(d\sqrt{1 - \alpha_n}/\xi_s)}, \quad (26)$$

where Eq. (19) is recovered in the limit $d\sqrt{1 - \alpha_n}/\xi_s \rightarrow 0$ and Eq. (25) is recovered in the limit $d\sqrt{1 - \alpha_n}/\xi_s \gg 1$. The full-field approximation for J_c given in Eq. (23) has the same leading-order monotonically decreasing behavior in low field as predicted by the authors of Refs. [16,17,43] using a model of an SNS Josephson junction from the linearized Usadel equations, including the applied magnetic field as an effective spin-flip scattering rate. Indeed, Eq. (23) can be viewed as an extension to this result that describes fields approaching the parallel critical field of the superconductor.

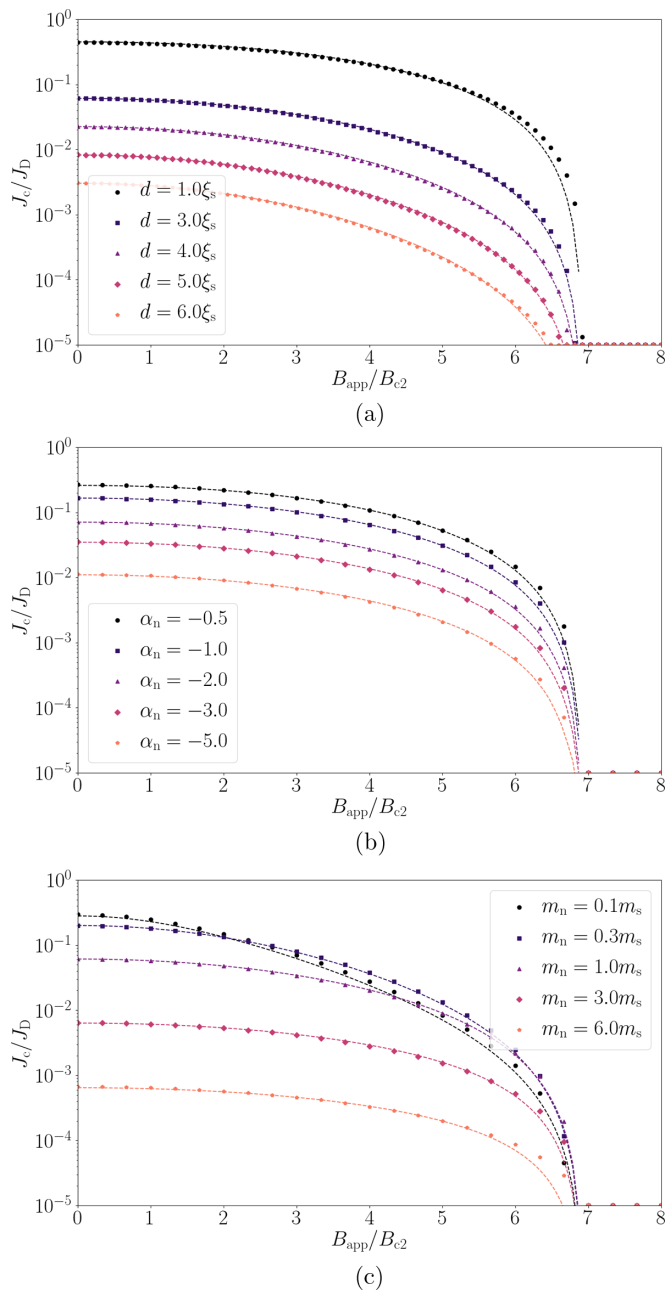


FIG. 6. Simulations of $J_c(B)$ for very narrow, thick, weakly coupled junctions. The width $w_s = 0.5\xi_s$, the periodic system length in the x direction $l = 12.0\xi_s$, and $\kappa = 5$. The grid spacing was $h_x = h_y = 0.1\xi_s$, the time step $\delta t = 0.5\tau$, and the hold time $t_{\text{hold}} = 5 \times 10^3\tau$. (a) The effective mass in the normal region was taken to be $m_n = m_s$, $\alpha_n = -1.0$, and the junction thickness d was varied. (b) $m_n = m_s$, α_n was varied, and $d = 2.0\xi_s$. (c) m_n was varied, $\alpha_n = -1.0$, and $d = 2.0\xi_s$. Dashed lines in all panels are given by Eq. (23).

Experimental measurements of SNS junctions consisting of superconducting nanowires in this monotonically decaying regime that have been carried out in Refs. [44,45] show good agreement with Eq. (23) for both the magnitude and magnetic field dependence, as shown in Fig. 7 with reasonable estimates for the coherence length in the superconducting nanowires. The approach provided here can be extended to consider thick

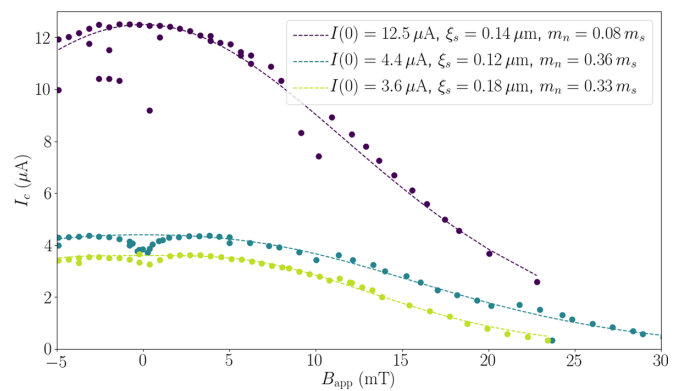


FIG. 7. Comparison of Eq. (23) with experimental data on Al-Au-Al nanowire junctions measured in Ref. [45]. The junction thickness d varied between 900 and 1300 nm, and all junctions were $w_s = 125$ nm wide. The coherence length ξ_n in the Au region was taken to be $10 \mu\text{m}$ as suggested by weak localization experiments below 50 mK. The critical current at zero field $I(0)$ was fixed at the maximum measured current, and the coherence length of the Al superconductor ξ_s and the ratio of the effective mass of a Cooper pair in Au and in Al, m_n/m_s , were left as free parameters for the fit.

clean junctions [46], but further work is needed to accurately describe the effective thickness of the barrier, when the long conduction-carrier scattering length in very clean barriers becomes comparable to the barrier's thickness.

B. Narrow junctions

We now extend our new solutions for $J_c(B_{\text{app}})$ in very narrow junctions to describe the qualitative behavior of wider 2D systems, so-called narrow junctions, with widths up to the length scale of the superconductor penetration depth λ_s , in arbitrary applied magnetic fields. In low fields, Eq. (13) accounts for the role of the phase in determining the equivalent fraction of the total width of the junction over which current density flows. This fraction follows from the distribution of vortices inside the junction and the (cancellation of) local currents flowing in opposite directions. The form of Eq. (13) can be compared with either the second Ginzburg-Landau equation in gauge-invariant form [Eq. (9)] or the Josephson relation $J = J_{\text{DJ}} \sin \Delta\varphi$ [40] (where the current density J between two points of interest is related to the gauge-invariant phase difference between them, $\Delta\varphi$). In both cases there are two factors, one associated with the magnitude of the order parameter and the other with phase. If we consider the Josephson relation averaged over the junction, we can replace the phase term with Clem's power-law term [Eq. (13)]. This ensures that $J_c(B_{\text{app}})$ reproduces Clem's results in low fields, when the applied field is far below the upper critical magnetic field of the junction. In high fields, the order parameter is depressed within the superconducting electrode, and we need a field-dependent form for J_{DJ} to account for this. In a narrow junction, both the order parameter and the local current density vary approximately on a length scale of the order of the vortex-vortex spacing a_0^* , instead of the junction width w_s . We therefore replace the zero-field J_{DJ} term in Eq. (13) with our new analytic field-dependent J_{DJ} expressions [Eqs. (19) and (23)] with the width w_s replaced by the vortex-vortex spacing.

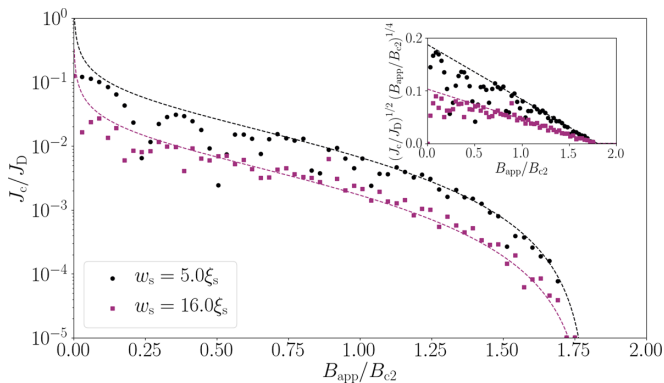


FIG. 8. Simulations of the critical current of a narrow, thin junction in the weak-coupling limit with the Ginzburg-Landau temperature parameter in the normal region $\alpha_n = -40.0$, a junction thickness $d = 0.25\xi_s$ smaller than the superconducting coherence length ξ_s , and a width w_s much smaller than the Josephson penetration depth λ_J but much larger than ξ_s . The periodic system size in the x direction $l = 100.0\xi_s$, and the Ginzburg-Landau parameter and friction coefficient in the superconductor are $\kappa = 40.0$ and $\eta = 5.79$, respectively, throughout. The grid spacing was chosen to be $h_x = h_y = 0.25\xi_s$, and the time step $\delta t = 0.5\tau$. Dashed lines represent Eq. (28) for the example parameters $B_{c2}^* = 1.8B_{c2}$ and $c_0 = c_1 = 0.58$. Remaining computational parameters are as described in the text. Inset: Kramer plot of data shown in the main plot.

This yields our approximation for J_c for narrow junctions over the full field range as

$$J_c(B_{\text{app}}) = c_0 \left(\frac{\phi_0}{B_{\text{app}} w_s^2} \right)^{c_1} J_{\text{DJ}}(B_{\text{app}}, w_s \rightarrow a_0^*), \quad (27)$$

where we set $q^2 = B_{\text{app}}/B_{c2}^*$ and J_{DJ} is taken to be Eq. (19) and Eq. (23) in the thin limit and in the thick limit, respectively. We have replaced B_{c2} by B_{c2}^* to include junctions such as that considered above, where there is an insulating surface barrier along the edge of both the superconductor and the junction and at fields between B_{c2}^* and B_{c2} current only flows along the edges [47]. In the case of a simple thin film between two insulators, the result $J_c \approx J_D(1 - B_{\text{app}}/B_{c2}^*)^{3/2}$ is obtained, as found previously by Abrikosov [48] and Boyd [49] close to the effective upper critical field of the system. For junctions with normal barrier coatings, $J_c(B_{\text{app}} = B_{c2}^*) = 0$ as required. In the weak-coupling limit, Eq. (27) for thin junctions takes the form

$$J_c(B_{\text{app}}) = J_0 \frac{c_0 \xi_s}{2d(1 - \alpha_n)} \left(\frac{\phi_0}{B_{\text{app}} w_s^2} \right)^{c_1} \left(1 - \frac{B_{\text{app}}}{B_{c2}^*} \right)^2, \quad (28)$$

whereas for thick junctions,

$$J_c(B_{\text{app}}) = J_0 \frac{c_0}{\sqrt{1 - \alpha_n}} \exp\left(-\frac{d\sqrt{1 - \alpha_n}}{\xi_s}\right) \times \left(\frac{\phi_0}{B_{\text{app}} w_s^2} \right)^{c_1} \left(1 - \frac{B_{\text{app}}}{B_{c2}^*} \right)^2. \quad (29)$$

Two-dimensional simulations for two narrow junctions in high field are plotted in Fig. 8 and compared with Eq. (28) with $c_0 = c_1 = 0.58$ and B_{c2}^* set to $1.8B_{c2}$. Excellent agreement is seen between the analytic functional form and the simulated

TABLE I. Material parameters for the reference 3D polycrystalline system for the 3D J_c investigations. J_c is decreased by 2.5% at each current step.

Parameter	Value
$h_{[x,y,z]}/\xi_s(T)$	0.5
$L_x/\xi_s(T)$	150.0
$L_y/\xi_s(T)$	150.0
$L_z/\xi_s(T)$	150.0
$D/\xi_s(T)$	22.4
$d_{\text{GB}}/\xi_s(T)$	0.5
α_{GB}	-2.0

data, with only B_{c2}^* taken as a free parameter. In this paper, we have not considered the very low field, self-field regime where the applied field is less than the applied field and $J_c(B_{\text{app}} \sim 0)$ is broadly field independent [50]. For the high-temperature superconductors, we also set aside magnetic fields close to B_{c2}^* , where variations in T_c and thermal activation play a role [51]. At intermediate fields (i.e., $B \sim B_{c2}^*/5$), Eqs. (28) and (29) both simplify to power-law behavior. For high-temperature superconductors, although there are a wide range of pinning landscapes that can produce a wide range of field dependencies [52], we note that power-law dependence with $c_1 \approx 0.6$ has been clearly observed in many powder-in-tube and tape high-temperature superconductors at intermediate magnetic fields [23,50,53,54].

V. 3D POLYCRYSTALLINE FLUX FLOW AND CRITICAL CURRENT SIMULATIONS

The morphology of grain boundaries in real 3D systems is significantly more complex than that considered in the 2D Josephson junction simulations of Sec. IV. Here, we investigate the critical current density that can be carried by a 3D polycrystalline system containing Josephson-junction-like grain boundaries using the TDGL-HI κ algorithm [25].

A. Polycrystalline simulations

To create our model polycrystalline material for critical current and flux pinning simulations, we first generate a 3D tessellation of equiaxed grains, periodic in all three dimensions, with grain sizes corresponding to a typical log-normal grain size distribution for a grain growth system, using the NEPER software package v3.5.0 [55,56].

For use as a simulation output, this tessellation is post-processed, with every mesh point in the superconducting volume within a distance $D/2$ of a face of a crystal grain assigned grain boundary properties with $\alpha = \alpha_{\text{GB}}$. In this manner, a rasterized approximation to an equiaxed polycrystal is constructed, with grain boundaries given degraded superconducting properties with $\alpha_{\text{GB}} < 1$. The base parameters of our model polycrystalline system are given in Table I. We consider Nb_3Sn at $T = 4.2$ K with a critical temperature of $T_{c,s} = 17.8$ K, a coherence length $\xi_s(4.2 \text{ K}) \approx 3.12$ nm, a size for the base system of $468 \times 468 \times 468$ nm, and a mean grain size $D = 70$ nm. An example distribution of grain boundaries for this set of parameters, along with distributions of

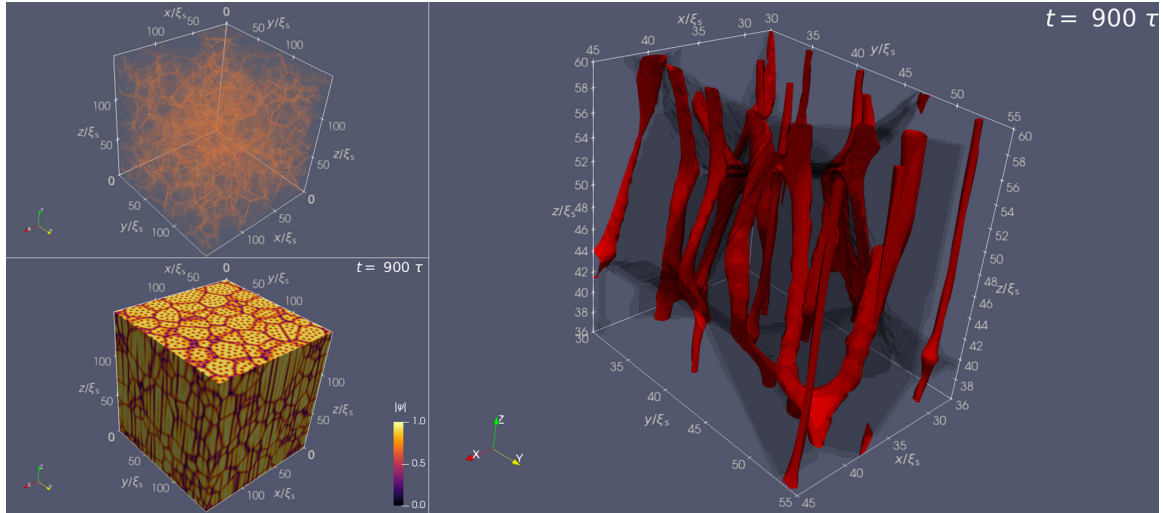


FIG. 9. A snapshot of the time-dependent simulation at $J_{\text{app}} = 10^{-2}J_D$ and $B_{\text{app}} = 0.2B_{c2}$ for the base system described in Table I. Top left: grain boundary network of the periodic physical system. Bottom left: distribution of the magnitude of the order parameter $|\psi|$ across the surfaces of the computational domain. The cores of the fluxons are clearly observable within the grains [64]. Right: distribution of vortices around an example grain in the system. The surface of the region enclosing points where $|\psi| < 0.25$ is displayed in red, and the grain boundary regions are shown in black.

$|\psi|$ over the simulation domain and close to a representative grain, is presented in Fig. 9. The flux pinning force per unit volume $F_p = J_c B_{\text{app}}$ as a function of reduced field, for polycrystalline material with different grain boundary parameters α_{GB} , obtained from TDGL-HI κ , is shown in Fig. 10(a). For consistency, we have confirmed that in homogeneous systems with no flux pinning structures present, no significant critical current densities are found in these simulations. The optimum flux pinning forces occur when the grain boundary thickness d_{GB} is close to the effective (normal metal) coherence length in the grain boundary $\xi_{\text{GB}} = \sqrt{-\alpha_{\text{GB}}\xi_s}$ (defined when $\alpha_{\text{GB}} < 0$), although we note that the spatial extent of the normal properties associated with the local strain and electronic properties of the grain boundary may extend well beyond its chemical or structural thickness [57]. For more degraded boundaries, J_c decays approximately exponentially at a rate proportional to $d_{\text{GB}}/\xi_{\text{GB}}$ for $d_{\text{GB}}/\xi_{\text{GB}} > 1$, and for $\alpha_{\text{GB}} < -4.0$ the maximum in the flux pinning force $F_p \propto J_c B_{\text{app}}$ is found at higher reduced field values. For more weakly degraded grain boundaries ($\alpha_{\text{GB}} > -4.0$), we find a Kramer dependence [18,58] such that the maximum flux pinning force per unit volume is close to $0.2B_{c2}$ and consistent with the field dependence of other computational results obtained using a different polycrystalline grain morphology [2]. Both the magnitude of J_c with a grain size of 70 nm at $10^{-3}J_D$ and the Kramer field dependence are similar to those observed experimentally in optimized polycrystalline Nb₃Sn [1] suggesting that the simulations capture the important physical processes in these systems. In the time-dependent simulations when $J > J_c$ (i.e., showing continuous vortex movement), we see significant differences in the curvature of moving vortices, above and below the optimum. In strongly degraded boundaries when $\alpha_{\text{GB}} < -4.0$, vortices are significantly curved and follow grain boundaries, being preferentially held at points where two or more grain boundaries meet, whereas for $\alpha_{\text{GB}} > -2.0$, vortices remain mostly straight, aligned along the applied field

in the z axis. Experimental and simulation flux pinning curves for different mean grain sizes are presented and compared in Fig. 11. In Fig. 11(b) the maximum flux pinning force per unit volume as a function of grain size is similar to the experimental values for $D > 100$ nm. However, for very small grain sizes, our simulations show F_p^{max} values that are larger than observed in experiment. The reduction in J_c found in fine-grained materials has been noted before and was attributed to degraded grain boundaries, stress in the superconducting layer generated during the fabrication process, and/or degraded (off-stoichiometric) grains [59]. Our computational results (that show no such reduction) enable us to tune grain boundary properties and morphologies that provide estimates for improved small-grained polycrystalline materials. Although we have found similar field dependencies in 3D polycrystalline systems before [37], these simulations display the increase of F_p^{max} with decreasing grain size D in bulk materials. This qualitative agreement with experiment is important because historically, an increase in J_c for reduced grain size has been considered the primary signature of flux pinning.

B. Flux pinning in polycrystalline materials

The Kramer-like field dependence implied by Eq. (28) has been widely observed in low-temperature polycrystalline superconductors such as Nb₃Sn [20] up to B_{c2} , and the $w^{-1.2}$ factor in Eq. (27) is reminiscent of the inverse grain size dependence observed for J_c experimentally [60] and in our simulations (Fig. 11). Pinning functions similar to the Kramer field dependence, calculated for different pinning landscapes by researchers such as Hampshire and Taylor [61] and Dew-Hughes [62], have been used extensively for the last 50 years to describe experimental J_c data. This approach has had the long-standing limitation that the pinning parameters derived in such analysis cannot easily be related to local properties of grain boundaries. Motivated by such considerations, we

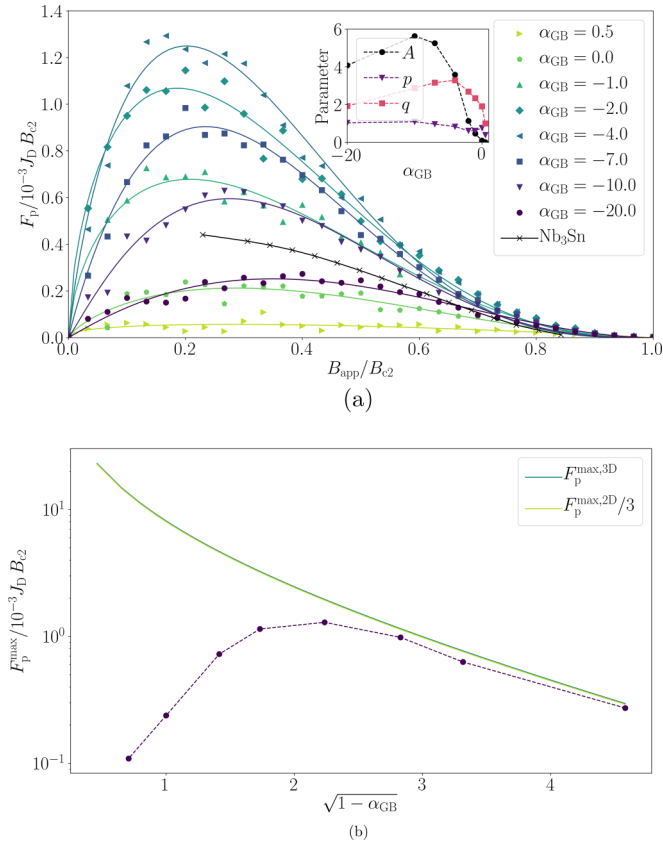


FIG. 10. (a) Normalized flux pinning force $F_p/10^{-3}J_D B_{c2}$ for the polycrystalline 3D system described in Table I with varying α_{GB} at various applied magnetic fields. The maximum in the flux pinning force is found close to $B_{app} = 0.2B_{c2}$ for $\alpha_{GB} > -4.0$ but moves to higher fields as the grain boundaries become more strongly normal (as α_{GB} decreases). Solid lines are fits to Eq. (30) with $r = 1.1$. Crosses represent a comparison with typical experimental data for bronze-route Nb_3Sn , taken from Ref. [1]. Inset: fitting parameters for Eq. (30) as a function of α_{GB} . (b) Maximum flux pinning force $F_p^{max}/J_D B_{c2}$ as a function of $\sqrt{1 - \alpha_{GB}}$. Line fits are comparisons with Eq. (30) with $A = 0.25$, $r = 0.6$, $p = 0.5$, and $q = 2$, and with Eq. (27).

propose an expression for the flux pinning force per unit volume for a polycrystalline system with weakly coupled grains (with highly degraded grain boundaries) based on Eq. (27) that enables comparison between the results provided here with a functional form similar to the widely used flux pinning formalism, where

$$F_p(B_{app}) \approx J_0 B_{c2} A \left(\frac{\phi_0}{B_{c2}^* D^2} \right)^r (b^*)^p (1 - b^*)^q f(\alpha_{GB}) \quad (30)$$

and we have replaced w_s by the grain size D , defined the pinning parameters $p \approx 1 - c_1$ and $q \approx 2$, introduced the new empirical parameters A and r , and made the weak-coupling approximations that $f(\alpha_{GB}) = \xi_s/2d(1 - \alpha_{GB})$ in the thin limit and $f(\alpha_{GB}) = \exp(-d\sqrt{1 - \alpha_{GB}}/\xi_s)/\sqrt{1 - \alpha_{GB}}$ in the thick-junction limit for the grain boundary (GB). The empirical parameters A and r account for the fraction of the total vortex length that is held within grain boundaries. F_p^{max} is found as usual at the field $b^* = p/(p + q)$. In standard flux

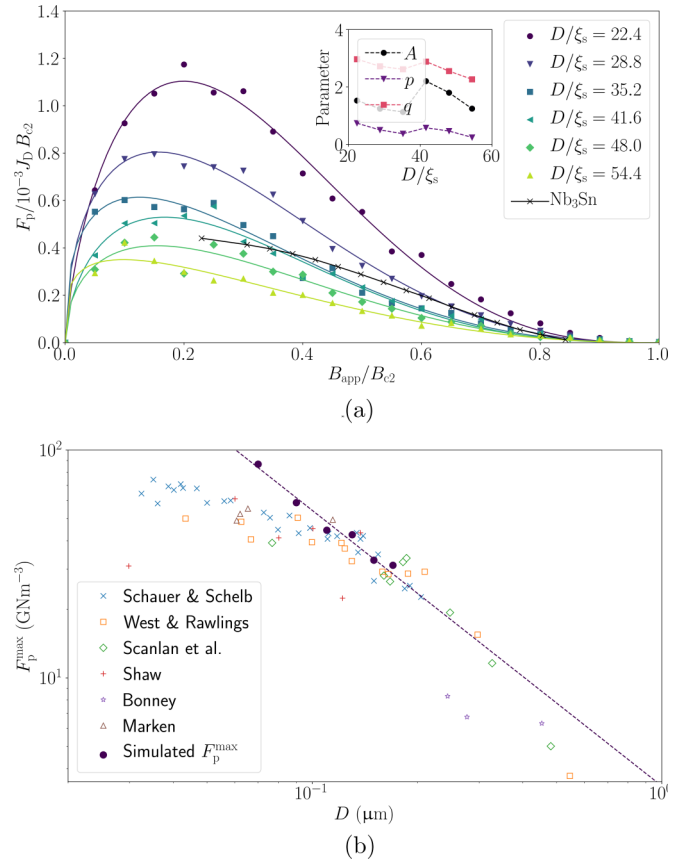


FIG. 11. (a) Normalized flux pinning force $F_p/10^{-3}J_D B_{c2}$ for a polycrystalline 3D system with varying mean grain size D . All other system parameters are set to the values given in Table I. Solid lines are fits to Eq. (30) with $r = 1.1$. Crosses represent a comparison with typical experimental data for bronze-route Nb_3Sn , taken from Ref. [1]. Inset: critical current density J_c as a function of applied field for varying grain size. (b) Maximum flux pinning force F_p^{max} compared with experimental data for the maximum flux pinning force measured in experimental Nb_3Sn samples taken from Ref. [65]. The dashed line represents the fit to Eq. (30) with $p = 0.5$ and $q = 2$ with remaining free parameters found to be $A = 0.09$ and $r = 0.6$. Experimental data as collected in [65] from: Schauer and Schelb [59], West and Rawlings [66], Scanlan *et al.* [67], Shaw [68], Bonney [69], and Marken [70].

pinning analysis, p and q are usually expected to be constant for a single flux pinning mechanism [63]. Figures 10 and 11 show that these parameters can vary significantly among materials that have a single grain boundary mechanism operating.

Comparisons of Eq. (30) in the thick-junction limit with our TDGL results are presented in Figs. 10(a) and 11(a). A , p , and q were taken to be free parameters for each flux pinning curve, and $r = 1.1$ was obtained as a global fit parameter from the combined set of simulations. The maximum in the flux pinning force per unit volume, F_p^{max} , has been compared with a constrained form of Eq. (30) in Figs. 10(b) and 11(b), in which the pinning parameters are restricted to their Kramer-like values $p = 0.5$, $q = 2$. The decrease in critical current density as the grain boundary properties degrade (as $\sqrt{1 - \alpha_{GB}}$ increases) in the weak-coupling limit of grains

appears to be well represented by Eq. (30) and $f(\alpha_{GB})$ taken from Eq. (25). In this case, the parameters A and r are closely related to their 2D equivalents in Eq. (29), with $r \approx c_1 \approx 0.6$ and in the limit of strongly degraded grain boundaries, $A \approx c_0/3$, as shown by Fig. 10. The observation that the prefactor c_0 in the 2D junction simulations is approximately three times larger than the prefactor A in the 3D simulations here may partly be due to the stronger surface barrier existing in the junction system at the junction-insulator interface. The surface barrier at the grain-grain boundary interface in the 3D simulations is generally weaker as a result of the proximity effect limiting supercurrents at the interface, similar to the effect observed at metallic interfaces. For the polycrystal system in Table I, which lies close to the peak $F_{p,max}$ in Fig. 11, $J_c \sim b^{-0.4}(1-b)^{2.7}$ ($p = 0.6$, $q = 2.7$), close to the Kramer-like field dependence of the critical current density $J_c \sim b^{-0.5}(1-b)^2$ ($p = 0.5$, $q = 2$). Deviations of p and q from predictions can occur due to multiple pinning mechanisms contributing to J_c concurrently; indeed, videos of the simulated vortex state in motion (not shown here) show complex vortex depinning from grain boundaries, line intersections, and triple points across the range of α_{GB} in Fig. 10.

VI. DISCUSSION AND CONCLUSIONS

It is important to note that all the polycrystalline simulations carried out in this work are in the high- κ limit, when the local magnetic field is equal to the applied magnetic field in the system at every point. Nevertheless, we expect the results to be qualitatively accurate for real systems of materials such as Nb₃Sn, since the penetration depth in such materials $\lambda_s \approx 100$ nm is still of the order of the grain size [1], and so in high fields, the field from the magnetization of grains will still be small relative to the applied magnetic field. The same is not necessarily true in very weak applied fields though, and thus care should be taken interpreting results in weak applied fields as a result. Nevertheless, large-scale TDGL simulations

provide an essential complementary tool for time-consuming and expensive experiments studying systematic variations in grain size in real materials. We derived expressions for the critical current density as a function of field from a junction-based model, used physical arguments to extend their range of validity, and confirmed the results obtained using TDGL. The equations obtained qualitatively agree with experimental data for polycrystalline superconductors such as Nb₃Sn and existing models based on flux shear through grain boundaries [60]. We have also performed 3D simulations of equiaxed polycrystalline systems in the high- κ limit, which show, for a complex polycrystalline system, an increase in the critical current density of the system with decreasing grain size in qualitative agreement with experiment [59]. Such simulations predict that maximum critical currents are achieved when the grain boundary thickness is similar to the effective coherence length in the grain boundary region.

Data are available on the Durham Research Online website [71]. The code is available on request from D.P.H.

ACKNOWLEDGMENTS

This work is funded by EPSRC Grant No. EP/L01663X/1, which supports the EPSRC Centre for Doctoral Training in the Science and Technology of Fusion Energy. This work has been carried out within the framework of the EUROfusion Consortium and has received funding from the Euratom Research and Training Programme 2014–2018 under Grant Agreement No. 633053. This work made use of the facilities of the Hamilton HPC Service of Durham University. The authors would like to thank M. Raine, A. Smith, J. Greenwood, S. Chislett-McDonald, C. Gurnham, B. Din, and P. Branch in Durham and E. Surrey and F. Schoofs at UKAEA for their support and useful discussions. One of the authors (DPH) would like to acknowledge the many tutorials, discussions and generosity of spirit from J. R. Clem and A. Campbell.

-
- [1] G. Wang, M. J. Raine, and D. P. Hampshire, How resistive must grain-boundaries be to limit J_c in polycrystalline superconductors? *Supercond. Sci. Technol.* **30**, 104001 (2017).
 - [2] G. J. Carty and D. P. Hampshire, Visualising the mechanism that determines the critical current density in polycrystalline superconductors using time-dependent Ginzburg-Landau theory, *Phys. Rev. B* **77**, 172501 (2008).
 - [3] A. Gurevich and L. D. Cooley, Anisotropic flux pinning in a network of planar defects, *Phys. Rev. B* **50**, 13563 (1994).
 - [4] D. P. Hampshire and S.-W. Chan, The critical current density in high fields in epitaxial thin films of YBa₂Cu₃O₇: Flux pinning and pair-breaking, *J. Appl. Phys. (Melville, NY)* **72**, 4220 (1992).
 - [5] P. Sunwong, J. Higgins, Y. Tsui, M. Raine, and D. P. Hampshire, The critical current density of grain boundary channels in polycrystalline HTS and LTS superconductors in magnetic fields, *Supercond. Sci. Technol.* **26**, 095006 (2013).
 - [6] L. Dobrosavljević-Grujić and Z. Radović, Magnetic field dependence of the critical currents in high T_c superconductors, *Phys. C (Amsterdam)* **185**, 2313 (1991).
 - [7] L. Dobrosavljević-Grujić and Z. Radović, Critical currents in superconductor-normal metal-superconductor junctions, *Supercond. Sci. Technol.* **6**, 537 (1993).
 - [8] J. R. Clem, Josephson junctions in thin and narrow rectangular superconducting strips, *Phys. Rev. B* **81**, 144515 (2010).
 - [9] K. K. Likharev, Superconducting weak links, *Rev. Mod. Phys.* **51**, 101 (1979).
 - [10] M. Moshe, V. G. Kogan, and R. G. Mints, Edge-type Josephson junctions in narrow thin-film strips, *Phys. Rev. B* **78**, 020510(R) (2008).
 - [11] G. R. Berdiyrov, M. V. Milošević, L. Covaci, and F. M. Peeters, Rectification by an Imprinted Phase in a Josephson Junction, *Phys. Rev. Lett.* **107**, 177008 (2011).
 - [12] G. R. Berdiyrov, A. R. de C. Romaguera, M. V. Milošević, M. M. Doria, L. Covaci, and F. M. Peeters, Dynamic and static phases of vortices under an applied drive in a superconducting stripe with an array of weak links, *Eur. Phys. J. B* **85**, 130 (2012).

- [13] G. Kimmel, I. A. Sadovskyy, and A. Glatz, *In silico* optimization of critical currents in superconductors, *Phys. Rev. E* **96**, 013318 (2017).
- [14] A. E. Koshelev, I. A. Sadovskyy, C. L. Phillips, and A. Glatz, Optimization of vortex pinning by nanoparticles using simulations of the time-dependent Ginzburg-Landau model, *Phys. Rev. B* **93**, 060508(R) (2016).
- [15] H. J. Fink, Supercurrents through superconducting-normal-superconducting proximity layers. I. Analytic solution, *Phys. Rev. B* **14**, 1028 (1976).
- [16] F. S. Bergeret and J. C. Cuevas, The vortex state and Josephson critical current of a diffusive SNS junction, *J. Low Temp. Phys.* **153**, 304 (2008).
- [17] J. C. Cuevas and F. S. Bergeret, Magnetic Interference Patterns and Vortices in Diffusive SNS Junctions, *Phys. Rev. Lett.* **99**, 217002 (2007).
- [18] E. J. Kramer, Scaling laws for flux pinning in hard superconductors, *J. Appl. Phys. (Melville, NY)* **44**, 1360 (1973).
- [19] D. M. J. Taylor and D. P. Hampshire, The scaling law for the strain dependence of the critical current density in Nb₃Sn superconducting wires, *Supercond. Sci. Technol.* **18**, S241 (2005).
- [20] S. A. Keys and D. P. Hampshire, A scaling law for the critical current density of weakly and strongly-coupled superconductors, used to parameterise data from a technological Nb₃Sn strand, *Supercond. Sci. Technol.* **16**, 1097 (2003).
- [21] S. A. Keys, N. Koizumi, and D. P. Hampshire, The strain and temperature scaling law for the critical current density of a jelly-roll Nb₃Al strand in high magnetic fields, *Supercond. Sci. Technol.* **15**, 991 (2002).
- [22] N. Cheggour, M. Decroux, Ø. Fischer, and D. P. Hampshire, Irreversibility line and granularity in Chevrel phase superconducting wires, *J. Appl. Phys. (Melville, NY)* **84**, 2181 (1998).
- [23] L. Le Lay, C. M. Friend, T. Maruyama, K. Osamura, and D. P. Hampshire, Evidence that pair breaking at the grain boundaries of Bi₂Sr₂Ca₂Cu₃O_x tapes determines the critical current density above 10 K in high fields, *J. Phys.: Condens. Matter* **6**, 10053 (1994).
- [24] N. B. Kopnin, *Theory of Nonequilibrium Superconductivity* (Oxford University Press, Oxford, 2009).
- [25] I. A. Sadovskyy, A. E. Koshelev, C. L. Phillips, D. A. Karpeyev, and A. Glatz, Stable large-scale solver for Ginzburg-Landau equations for superconductors, *J. Comput. Phys.* **294**, 639 (2015).
- [26] J. Fleckinger-Pelle and H. G. Kaper, Gauges for the Ginzburg-Landau equations of superconductivity, Report No. ANL/MCS/CP-87416, Argonne National Laboratory, Lemont, IL (1995).
- [27] A. Schmid, A time dependent Ginzburg-Landau equation and its application to the problem of resistivity in the mixed state, *Phys. Kondens. Mater.* **5**, 302 (1966).
- [28] P. G. de Gennes, *Superconductivity of Metals and Alloys* (Perseus Books, Boulder, CO, 1999).
- [29] S. J. Chapman, Q. Du, and M. D. Gunzburger, A Ginzburg-Landau type model of superconducting/normal junctions including Josephson junctions, *Eur. J. Appl. Math.* **6**, 97 (1995).
- [30] S. J. Chapman, Superheating field of Type-II superconductors, *SIAM J. Appl. Math.* **55**, 1233 (1995).
- [31] T. Winiecki and C. S. Adams, A fast semi-implicit finite difference method for the TDGL equations, *J. Comput. Phys.* **179**, 127 (2002).
- [32] W. D. Gropp, H. G. Kaper, G. K. Leaf, D. M. Levine, M. Palumbo, and V. M. Vinokur, Numerical simulation of vortex dynamics in Type-II superconductors, *J. Comput. Phys.* **123**, 254 (1996).
- [33] W. F. Ames, *Numerical Methods for Partial Differential Equations* (Academic, San Diego, CA, 1992).
- [34] T. Boutboul, V. Abaecherli, G. Berger, D. P. Hampshire, J. Parrell, M. J. Raine, P. Readman, B. Sailer, K. Schlenga, M. Thoenner, E. Viladiu, and Y. Zhang, European Nb₃Sn superconducting strand production and characterization for ITER TF coil conductor, *IEEE Trans. Appl. Supercond.* **26**, 6000604 (2016).
- [35] W. H. Press, B. P. Flannery, S. A. Teukolsky, and W. T. Vetterling, *Numerical Recipes in Fortran: The Art of Scientific Computing*, 2nd ed. (Cambridge University Press, Cambridge, 1992).
- [36] I. A. Sadovskyy, A. E. Koshelev, W.-K. Kwok, U. Welp, and A. Glatz, Targeted evolution of pinning landscapes for large superconducting critical currents, *Proc. Natl. Acad. Sci. USA* **116**, 10291 (2019).
- [37] G. J. Carty and D. P. Hampshire, The critical current density of an SNS junction in high magnetic fields, *Supercond. Sci. Technol.* **26**, 065007 (2013).
- [38] I. A. Sadovskyy, A. E. Koshelev, A. Glatz, V. Ortalan, M. W. Rupich, and M. Leroux, Simulation of the Vortex Dynamics in a Real Pinning Landscape of YBa₂Cu₃O_{7- δ} Coated Conductors Coated Conductors, *Phys. Rev. Appl.* **5**, 014011 (2016).
- [39] J. R. Clem, Effect of nearby Pearl vortices upon the I_c versus B characteristics of planar Josephson junctions in thin and narrow superconducting strips, *Phys. Rev. B* **84**, 134502 (2011).
- [40] A. F. Volkov, Theory of the current-voltage characteristics of one-dimensional S-N-S and S-N junctions, *Sov. Phys. JETP* **39**, 366 (1974).
- [41] M. Tinkham, *Introduction to Superconductivity*, 2nd ed. (McGraw-Hill, Singapore, 1996).
- [42] P. G. de Gennes, Boundary effects in superconductors, *Rev. Mod. Phys.* **36**, 225 (1964).
- [43] J. C. Hammer, J. C. Cuevas, F. S. Bergeret, and W. Belzig, Density of states and supercurrent in diffusive SNS junctions: Roles of nonideal interfaces and spin-flip scattering, *Phys. Rev. B* **76**, 064514 (2007).
- [44] F. Chiodi, M. Ferrier, S. Guéron, J. C. Cuevas, G. Montambaux, F. Fortuna, A. Kasumov, and H. Bouchiat, Geometry-related magnetic interference patterns in long SNS Josephson junctions, *Phys. Rev. B* **86**, 064510 (2012).
- [45] L. Angers, F. Chiodi, G. Montambaux, M. Ferrier, S. Guéron, H. Bouchiat, and J. C. Cuevas, Proximity dc squids in the long-junction limit, *Phys. Rev. B* **77**, 165408 (2008).
- [46] T. Y. Hsiang and D. K. Finnemore, Superconducting critical currents for thick, clean superconductor-normal-metal-superconductor junctions, *Phys. Rev. B* **22**, 154 (1980).
- [47] L. Burlachkov, A. E. Koshelev, and V. M. Vinokur, Transport properties of high-temperature superconductors: Surface vs bulk effect, *Phys. Rev. B* **54**, 6750 (1996).
- [48] A. A. Abrikosov, Concerning surface superconductivity in strong magnetic fields, *Sov. Phys. JETP* **20**, 480 (1965).
- [49] R. G. Boyd, Longitudinal critical current in Type-II superconductors, *Phys. Rev.* **145**, 255 (1966).
- [50] C. Gurnham and D. P. Hampshire, Self-field effects in a Josephson junction model for J_c in REBCO tapes, *IEEE Trans. Appl. Supercond.* **32**, 8000205 (2022).

- [51] M. Roulin, A. Junod, and E. Walker, Flux lattice melting transition in $\text{YBa}_2\text{Cu}_3\text{O}_{6.94}$ observed in specific heat experiments, *Science* **273**, 1210 (1996).
- [52] R. Willa, A. E. Koshelev, I. A. Sadovskyy, and A. Glatz, Strong-pinning regimes by spherical inclusions in anisotropic Type-II superconductors, *Supercond. Sci. Technol.* **31**, 014001 (2018).
- [53] P. Sunwong, J. S. Higgins, and D. P. Hampshire, Probes for investigating the effect of magnetic field, field orientation, temperature and strain on the critical current density of anisotropic high-temperature superconducting tapes in a split-pair 15 T horizontal magnet, *Rev. Sci. Instrum.* **85**, 065111 (2014).
- [54] C. Senatore, C. Barth, M. Bonura, M. Kulich, and G. Mondonico, Field and temperature scaling of the critical current density in commercial REBCO coated conductors, *Supercond. Sci. Technol.* **29**, 014002 (2016).
- [55] R. Quey, P. R. Dawson, and F. Barbe, Large-scale 3D random polycrystals for the finite element method: Generation, meshing and remeshing, *Comput. Methods Appl. Mech. Eng.* **200**, 1729 (2011).
- [56] R. Quey and L. Renversade, Optimal polyhedral description of 3D polycrystals: Method and application to statistical and synchrotron X-ray diffraction data, *Comput. Methods Appl. Mech. Eng.* **330**, 308 (2018).
- [57] H. Hilgenkamp and J. Mannhart, Grain boundaries in high- T_c superconductors, *Rev. Mod. Phys.* **74**, 485 (2002).
- [58] E. J. Kramer, Microstructure - critical current relationships in hard superconductors, *J. Electron. Mater.* **4**, 839 (1975).
- [59] W. Schauer and W. Schelb, Improvement of Nb_3Sn high field critical current by a two-stage reaction, *IEEE Trans. Magn.* **17**, 374 (1981).
- [60] D. Dew-Hughes, The role of grain boundaries in determining J_c in high-field high-current superconductors, *Philos. Mag. B* **55**, 459 (1987).
- [61] R. Hampshire and M. Taylor, Critical supercurrents and pinning of vortices in commercial Nb-60 at. percent Ti, *J. Phys. F: Met. Phys.* **2**, 89 (1972).
- [62] D. Dew-Hughes, Flux pinning mechanisms in Type II superconductors, *Philos. Mag.* **30**, 293 (1974).
- [63] D. Dew-Hughes and M. J. Witcomb, The effect of dislocation tangles on superconducting properties, *Philos. Mag.* **26**, 73 (1972).
- [64] D. Roditchev, V. Brun, L. Serrier-Garcia, J. C. Cuevas, V. H. L. Bessa, M. V. Milošević, F. Debontridder, V. Stolyarov, and C. Cren, Direct observation of Josephson vortex cores, *Nat. Phys.* **11**, 332 (2015).
- [65] L. A. Bonney, T. C. Willis, and D. C. Larbalestier, Dependence of critical current density on microstructure in the SnMo_6S_8 Chevrel-phase superconductor, *J. Appl. Phys. (Melville, NY)* **77**, 6377 (1995).
- [66] A. W. West and R. D. Rawlings, A transmission electron microscopy investigation of filamentary superconducting composites, *J. Mater. Sci.* **12**, 1862 (1977).
- [67] R. M. Scanlan, W. A. Fietz, and E. F. Koch, Flux pinning centers in superconducting Nb_3Sn , *J. Appl. Phys.* **46**, 2244 (1975).
- [68] B. J. Shaw, Grain size and film thickness of Nb_3Sn formed by solid-state diffusion in the range 650–800°C, *J. Appl. Phys.* **47**, 2143 (1976).
- [69] L. A. Bonney, Microstructural Dependence of Critical Current Densities in the SnMo_6S_8 Chevrel Phase Superconductor, Ph.D. thesis, University of Wisconsin-Madison, 1994.
- [70] K. Marken, Characterization Studies of Bronze-Process Filamentary Nb_3Sn Composites, Ph.D. thesis, University of Wisconsin-Madison, 1986.
- [71] <https://dro.dur.ac.uk>.